Review of Scientific Instruments

A cantilever torque magnetometry method for the measurement of Hall conductivity of highly resistive samples

Cite as: Rev. Sci. Instrum. **91**, 045001 (2020); https://doi.org/10.1063/1.5143451
Submitted: 23 December 2019 . Accepted: 19 March 2020 . Published Online: 06 April 2020

Samuel Mumford, Tiffany Paul, Seung Hwan Lee, Amir Yacoby, and Aharon Kapitulnik

Review of Scientific Instruments ARTICLE scitation.org/journal/rsi

A cantilever torque magnetometry method for the measurement of Hall conductivity of highly resistive samples

Cite as: Rev. Sci. Instrum. 91, 045001 (2020); doi: 10.1063/1.5143451
Submitted: 23 December 2019 • Accepted: 19 March 2020 •
Published Online: 6 April 2020

Samuel Mumford,[1,2,a)] Tiffany Paul,[1,3] Seung Hwan Lee,[4] Amir Yacoby,[4] and Aharon Kapitulnik[1,2,3]

AFFILIATIONS

[1]Geballe Laboratory for Advanced Materials, Stanford University, Stanford, California 94305, USA
[2]Department of Physics, Stanford University, Stanford, California 94305, USA
[3]Department of Applied Physics, Stanford University, Stanford, California 94305, USA
[4]Department of Physics, Harvard University, Cambridge, Massachusetts 02138, USA

[a)]Author to whom correspondence should be addressed: smumfor2@stanford.edu

ABSTRACT

We present the first measurements of Hall conductivity utilizing a torque magnetometry method. A Corbino disk exhibits a magnetic dipole moment proportional to Hall conductivity when voltage is applied across a test material. This magnetic dipole moment can be measured through torque magnetometry. The symmetry of this contactless technique allows for the measurement of Hall conductivity in previously inaccessible materials. Finally, we calculate a low-temperature noise bound, demonstrate the lack of systematic errors, and measure the Hall conductivity of sputtered indium tin oxide.

I. INTRODUCTION

Measurements of transverse transport properties such as the Hall effect, Nernst effect, and transverse thermal conductivity have become of great importance in understanding modern quantum materials. However, such measurements are often made difficult, or even impossible, due to the contamination of longitudinal transport effects. For example, in a standard Hall bar measurement of the Hall effect, the transverse voltage $V_y(H)$ is measured in response to the application of a longitudinal current I_x in the presence of a perpendicular magnetic field $H\hat{Z}$ using two contacts on opposite sides of the sample [see Fig. 1(a)]. A common procedure to eliminate contributions from the longitudinal magnetoresistance due to contact misalignment invokes the odd symmetry of the effect to find the Hall resistance $\rho_{xy} = [V_y(H) - V_y(-H)]/2I_x$. (Here, we use the 2D notation where thickness is fixed.) However, this simple procedure often fails when $\rho_{xx} \gg \rho_{xy}$, such as the variable range hopping (VRH) regime of disordered insulators[1,2] or on the insulating side of superconductor–insulator transition.[3–7] Only a handful of Hall measurements were done in the VRH regime (see Refs. 8 and 9) despite detailed theories,[10,11] and, in general, measurements were restricted to the vicinity of the metal–insulator transition (MIT). The issue is complicated further if one is interested in the transverse conductivity σ_{xy}, which can be calculated from the resistivity tensor, but with uncontrolled error-bars if ρ_{xx} diverges. A direct measurement of σ_{xy} is needed to probe a variety of topological states of matter in the bulk material-system where edge states may dominate the transport. For example, standard transport approaches to measure the quantum Hall effect (QHE) in two-dimensional electron gas (2DEG) interact directly with the edge states, with no ability to explore the existence of Hall currents in the bulk of the sample.[12] Indeed, the original theoretical approach to explain the QHE by Laughlin[13] used a closed metallic ribbon configuration, equivalent to a Corbino disk,[14] to demonstrate the effect.

In this paper, we demonstrate a new method for measuring σ_{xy} in a Corbino disk configuration, where the induced Hall currents in the disk create a magnetic dipole moment that is measured by torque magnetometry. A circularly symmetric Corbino disk is shown in Fig. 1(b). Fabricated at the end of a cantilever, it forms the basis of this σ_{xy} measurement technique.[14] Applying a voltage V between

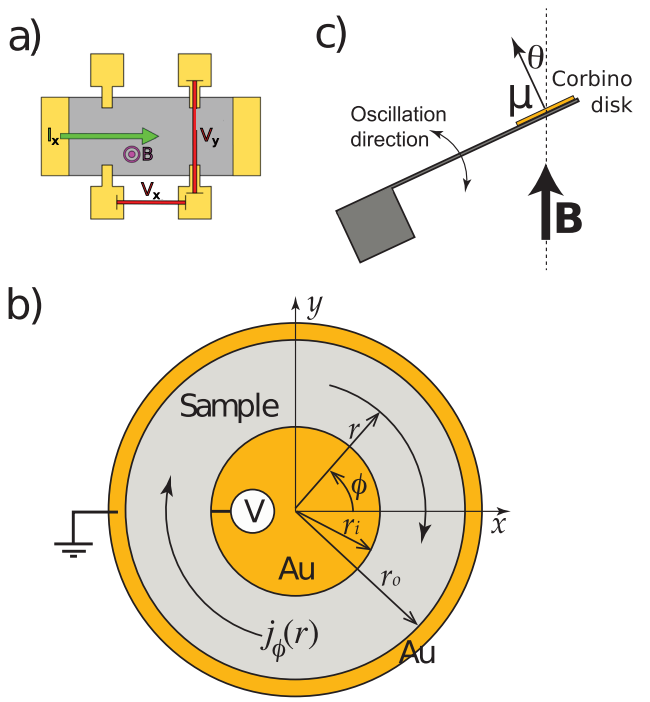

FIG. 1. (a) The typical Hall bar consists of four contacts and a drive current I. A symmetry-breaking magnetic field B allows non-diagonal terms in the resistivity tensor ρ. Correspondingly, there is a Hall voltage $V_y \propto \rho_{xy} I_x$ across contacts separated $\perp$ to I_x as well as the longitudinal voltage $V_x \propto \rho_{xx} I_x$. (b) Corbino disk configuration used for σ_{xy} measurements. Here, the Au metallic contacts serve as the equipotential rings. (c) Side view of torque magnetometry.

the inner and outer contacts creates a radial electric field E_r, which induces a circulating Hall current with a current density $j_\phi(r)$. This Hall current creates a magnetic dipole moment μ parallel to the ring normal, which can be directly evaluated by

$$\mu = \int j_\phi(r)\pi r^2 dr = \int \sigma_{xy} E_r \pi r^2 dr. \equiv \sigma_{xy} G V, \tag{1}$$

where G is a geometrical factor. For concentric rings, one obtains

$$\mu = \sigma_{xy} \frac{\pi(r_o^2 - r_i^2)}{2\ln(r_o/r_i)} V, \tag{2}$$

where r_i and r_o are the inner and outer radii of the test material, respectively. While real fabricated devices may deviate slightly from concentric rings, such errors are small on the scale of the full Corbino disk and an image of the device can be used to numerically correct that error.

The magnetic dipole moment is then measured by means of torque magnetometry, as shown in Fig. 1(c), which allows for a high-precision contactless measurement. The dipole moment is measured without placing elements in series with the Hall current, and the torque measurement is insensitive to higher order magnetic moments caused by misalignment. The magnetic dipole moment of the full Corbino disk is also relatively insensitive to local disorder sources. Moreover, as the Corbino disk torque must be linear in V and even in B, one may separate the signal due to the Hall effect from other effects due to cantilever heating or longitudinal current by signal symmetry. Additionally, while not discussed in the present manuscript, this method is easily generalized for the study of Nernst currents that are excited when a temperature gradient is applied between the inner and outer contacts. This temperature gradient can be easily realized using the same laser that is used to drive the cantilever discussed below.

II. METHODS

A. Measurement concept

Cantilever torque magnetometry utilizes a high-Q resonator to detect the interaction between a magnetic dipole and an external magnetic field.[15–17] The angular response θ of a cantilever with moment of inertia A, resonant frequency $\omega_0 = 2\pi f_0$, and quality factor Q subject to an external torque τ may be approximated as a damped harmonic oscillator by the following equation:[18]

$$A\ddot{\theta} + \frac{A}{Q}\omega_0\dot{\theta} + A\omega_0^2\theta = \tau. \tag{3}$$

An external magnetic field $\vec{B}$ exerts a torque[15]

$$\vec{\tau} = \vec{\mu} \times \vec{B}. \tag{4}$$

If the dipole moment and magnetic field are aligned in the cantilever equilibrium position, an effective detuning torque

$$\tau_D = \mu B \sin(\theta) \approx \mu B\theta \tag{5}$$

results as the cantilever oscillates. Inserting τ_D into Eq. (3) shifts the resonant frequency by

$$A\omega_0^2 \to A\omega_0^2 - \mu B \quad \text{or} \quad \frac{\Delta\omega_0}{\omega_0} = \frac{\mu B}{2A\omega_0^2}. \tag{6}$$

Using Eq. (2), the shift in the resonant frequency can be related to the applied voltage, magnetic field, and σ_{xy} by

$$\delta f_0 = \frac{GV}{8\pi^2 A f_0} B\sigma_{xy}. \tag{7}$$

Measurement of changes in f_0 of a patterned cantilever with voltage therefore probes σ_{xy} without polluting terms from ρ_{xx}.

B. Device fabrication

Corbino disks were patterned on high-Q single-crystal silicon cantilevers, as shown in Fig. 2. Fabrication was performed using photolithography as all features are larger than 15 μm. Fabrication began with a silicon on insulator (SOI) wafer with a 450 μm handle layer, a 4 μm buried oxide layer, and a 2 μm or 3 μm device layer of (001) Si depending on the design. A CVD SiO_2 layer was first deposited onto the handle side, and this oxide was plasma etched in an array of square windows. Next, 25 nm of Ti–Pt was patterned in the shape of the cantilever on the device side. This conductive layer serves as a ground plane and separates the Corbino disk voltages from the underlying Si. A 40 nm thick barrier of ALD HfO_2 and CVD nitride was then grown on top of the Pt to electrically separate the grounding plane from the subsequently deposited layers. On the

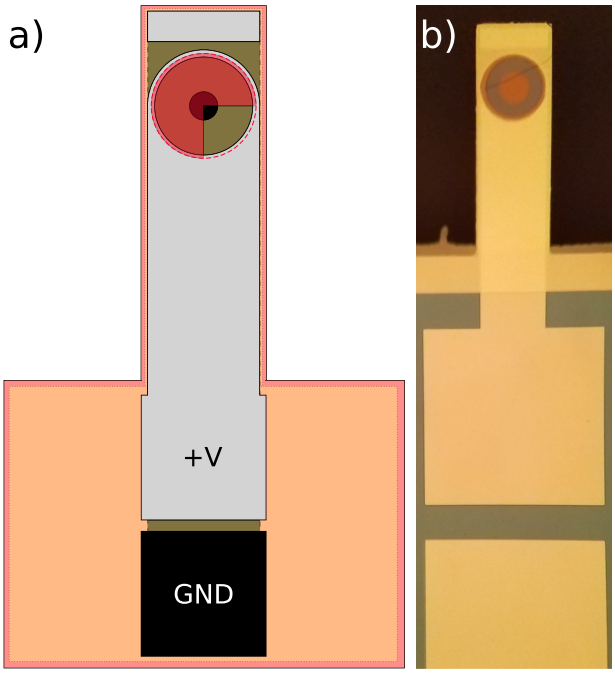

FIG. 2. (a) Schematic drawing of a cantilever patterned with a Corbino disk in the planar coaxial design. An insulating barrier (orange) separates the Pt inner contact (black) and the Pt outer ring contact (gray). The test material (red) is deposited in a circle connecting the voltage contacts, and the underlying Si is shown in pink. (b) A planar coaxial Corbino disk cantilever with ITO as the test material.

planar coaxial design shown in Fig. 2, a hole was etched in this insulating layer for the grounded central Corbino disk contact and the Pt outer contact was deposited directly onto the SiN–HfO_2 insulating layer. The ground plane serves both as the inner contact and as a conductive barrier in the planar coaxial design. The cantilever shape was etched out from the device layer Si using a Bosch etcher. Finally, the test material was deposited between the inner and outer contacts, and the cantilever was released using a backside Bosch etch and a final oxide plasma etch.

For devices with separate grounded wires on top of the ground plane, such as the Ge dummy device of Sec. III C, the SiN–HfO_2 insulating barrier was not etched. A thin Ti–Au inner contact was instead deposited onto this insulating substrate, and a 20 nm thick ALD HfO_2 ring was patterned to cover most of this inner contact. This ring separates the inner and outer voltage contacts. The resulting cantilevers with separate ground planes are $250 \times 600 \times 3\ \mu m^3$ with $f_0 \sim 10$ kHz. The planar coaxial design cantilevers are $200 \times 600 \times 2\ \mu m^3$ with $f_0 \sim 7$ kHz. Both exhibit $Q \sim 300\,00$ at pressures below 1×10^{-5} Torr, which does not change significantly in the magnetic field.

To avoid competing signals, all device patterns used in this study were designed to exactly null any possible current loop perpendicular to the magnetic field. However, using optical masks, an unavoidable misalignment is estimated to result in an effective loop area of not more than 200 μm^2. With a typical current of 3×10^{-4} A, this translates to a residual moment $\mu_{res} \sim 10^{-13}$ A m^2 and a linear in B contribution to $\delta\omega_0$ by Eq. (6). The linear signal is clearly seen in our results below. As the misalignment signal is odd in the magnetic field, it can be separated from the Hall moment signal, which is even in the magnetic field. Such a process is analogous to flipping the sign of B and looking for an odd component in V_y in a Hall bar, but in this case, the polluting linear signal becomes smaller as ρ_{xx} increases. Future devices can be fabricated using e-beam lithography to render this contribution negligible.

C. Interferometric resonant frequency detection

The resonant frequency of the cantilever is tracked with a fiber interferometer. The output of a 1310 nm fiber-coupled laser diode is first fed through a 90-10 splitter. The majority of the laser power goes to a reference photodiode, and the remaining 10% of the laser power is connected to a cleaved fiber optic cable. The cleaved fiber end is then aligned over a cantilever to form an interferometer, as shown in Fig. 3. The output from this interferometer is converted into a voltage by a photodiode and computer processed after analog-to-digital conversion. The interferometer voltage $V(t)$ for the laser wavelength λ, peak to peak voltage V_{pp}, and fiber–cantilever distance Δz is

$$V(t) \approx \frac{2\pi V_{pp}\Delta z(t)}{\lambda} \sin\left(\frac{4\pi\Delta z_0}{\lambda}\right) \propto \Delta z(t). \tag{8}$$

The fiber interferometer thus provides the means to precisely track cantilever motion.

The cantilever resonant frequency is measured by observing the response to a radiation pressure drive. A 1550 nm fiber coupled laser is connected to the cleaved fiber used for interferometry. The power of this laser is reflected off of a Pt pad near the end of the cantilever. This laser power is modulated with a frequency sweeping voltage over a frequency width δf and time t_{sw},

$$V_{sw} = V_0 \sin\left[2\pi\left(f_0 - \frac{\delta f}{2} + \frac{\delta f t}{2t_{sw}}\right)t\right], \tag{9}$$

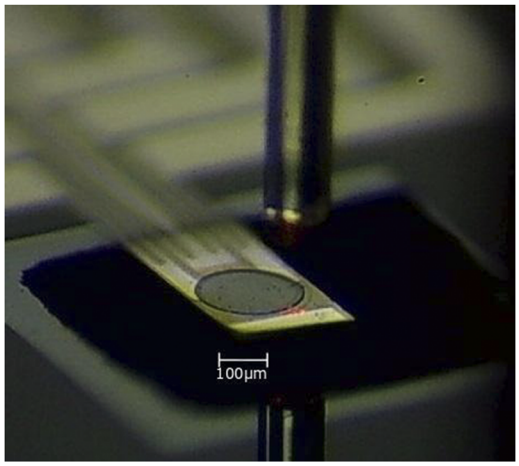

FIG. 3. A cleaved fiber above a cantilever forming an interferometer. The two interfering light sources are the reflected light from the fiber end and the cantilever surface. The fiber was aligned with a three-axis stage and a red laser before being epoxied to the cantilever wafer. A separate pad of Pt was patterned on the end of the cantilever for alignment.

to create a sweeping radiation pressure drive. The sweeping drive voltage is also connected to a reference port in the analog-to-digital converter to fit for the cantilever response function, as shown in Fig. 4.

The shape of the cantilever response function to the applied laser drive is fit for ω_0 and Q, and the amplitude of the response is used to calculate A, as shown in Appendix B. Note that such a calculation of A assumes that all laser light is normal to the cantilever surface and that it is reflected. As a result, all calculations of A are lower bounds, and the corresponding calculations of torques are similarly lower bounds. With improvements to the electronics, A could be calculated without this assumption using the undriven cantilever motion through equipartition.

As shown in Appendix A, the minimum detectable shift in the resonant frequency for a cantilever with the length L and vibrational temperature T driven for time t_{samp} is

$$\frac{\Delta\omega_0}{\omega_0} = \frac{2L}{\lambda}\sqrt{\frac{2k_bT\pi}{A\omega_0^3 t_{samp}Q}}, \tag{10}$$

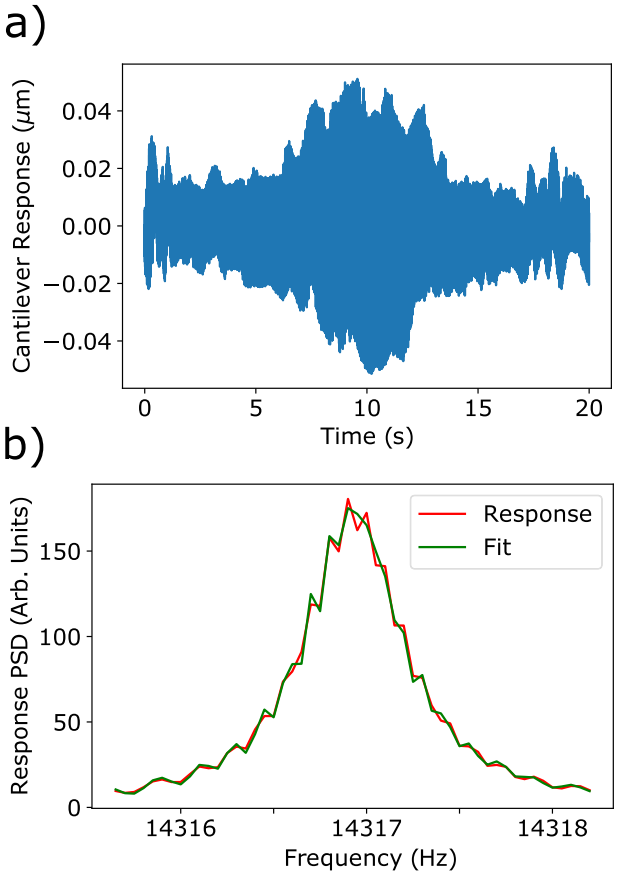

FIG. 4. (a) Real time response of a 3 μm thick Si cantilever to a sweep drive. The amplitude of driving power modulation was 50 μW. Each drive and fit was performed over 20 s, so subsequent drives would be independent with a cantilever response time of ~2 s. (b) Power spectral density of the cantilever response seen in part (a). Response is fit to a damped harmonic oscillator equation finding f_0 of 14 316.9 Hz and a Q of 230 00.

which by Eqs. (2) and (6) translates to a minimum detectable σ_{xy} of

$$\delta\sigma_{xy} = \frac{4L\ln(r_o/r_i)}{\lambda(r_o^2 - r_i^2)VB}\sqrt{\frac{2k_bTA\omega_0}{\pi t_{samp}Q}}. \tag{11}$$

For this cantilever design, a dilution refrigerator temperature of 0.1 K, a 5 T magnet, and 0.1 V applied, the minimum detectable $\sigma_{xy} \sim 10^{-11}\ \Omega^{-1}$. Such uncertainty improves upon Hall bar measurements by a factor of $>10^6$ for insulating samples extrapolated to $T \to 0$.[19] Note that as sample heating scales as V^2/ρ, the minimum observable σ_{xy} scales as $1/\sqrt{\rho}$ and decreases dramatically for insulators at low temperature.

III. EXPERIMENTAL RESULTS

A. Torque detection test: CGT and $RuCl_3$

A flake of $Cr_2Ge_2Te_6$ (CGT) was placed on a single crystal Si cantilever with patterned Pt wires, as shown in Fig. 5. CGT flakes were placed on the released cantilevers using thin gold wires and glued using Stycast 1266 epoxy. CGT is studied as a van der Waals ferromagnet with a bulk transition temperature T_c of ~65 K.[20] Here, CGT is used as a reference measurement for sensing δf_0 and serves as a test of the patterned cantilever design and data taking procedure.

A clear magnetic response in f_0 is observed both as a function of temperature and magnetic field. As seen in Fig. 6(a), there is a quadratic response in $f_0(B)$ below T_c. A resistive heater was then used to profile the magnetic response across the transition temperature, as seen in Fig. 6(b). The clear emergence of the magnetic response at the transition temperature of 63.77 ± 0.1 K demonstrates both temperature control in the system and that in the observed $\delta f_0(B)$ can be attributed to the CGT instead of systematic effects or magnetization of other cantilever components. This procedure was repeated to find a kink in the magnetic susceptibility of $RuCl_3$[21] at 14 K, as seen in Fig. 6(c).

Finally, using the observed $A = 1.6 \times 10^{-18}$ kg m^2 for the $RuCl_3$ flake cantilever and uncertainty in f_0 with one hour of averaging time of 0.1 mHz, the minimum detectable dipole moment is $4 \times 10^6 \mu_B$ at $B = 1$ T. Such a precision represents a modest improvement in sensitivity over other resonant torque magnetometry approaches[22] and demonstrates that f_0 may be tracked interferometrically on cantilevers with additional patterned layers.

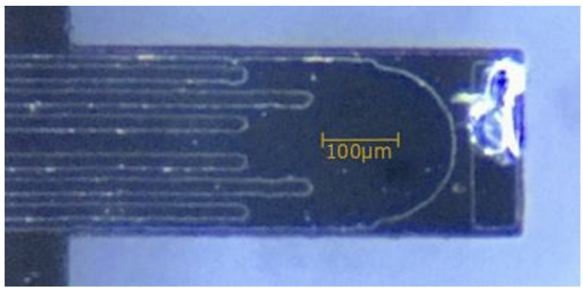

FIG. 5. A single crystal silicon cantilever with an attached CGT flake on the interferometric aligning pad.

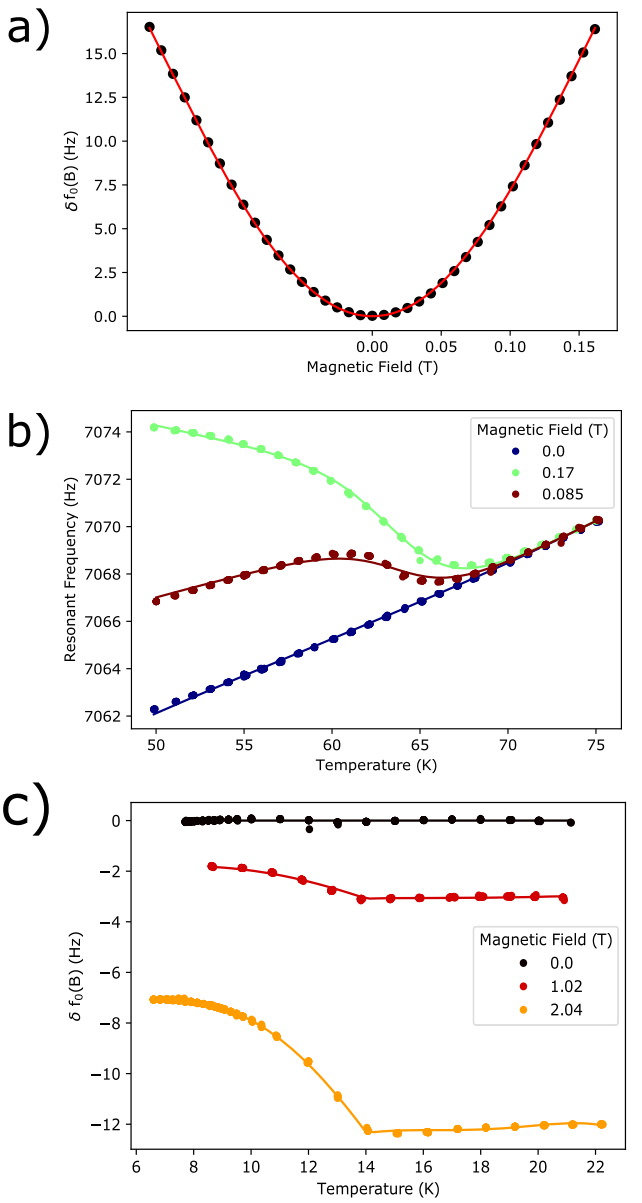

FIG. 6. (a) The magnetic response of the cantilever f_0 due to a CGT flake at the probe base temperature of 5 K. Note the small magnetic field used, remaining below the coercive field of CGT due to the large amplitude of $\delta f_0(B)$. (b) Tracking the resonant frequency of CGT across the transition temperature as a function of magnetic field. Note that above T_c, the resonant frequency is magnetic field-independent and a clear magnetic response appears at the transition temperature. (c) Magnetic field dependent shift in the resonant frequency of a cantilever with a $RuCl_3$ flake. Note the kink in magnetic susceptibility at 14 ± 0.1 K.

B. Systematics tests: Conductive Pt device

Dummy devices that should not exhibit a Hall signal were investigated to check for systematic errors. An initial dummy device consisted of a Corbino disk with Pt as the test material patterned on a 3 μm thick single-crystal Si cantilever, as shown in Fig. 7(a). Note that this design is identical to the later cantilevers, which exhibit the Hall signal except for the Pt used as the test material. The resistance of the Pt wires was 110 Ω, and alternating voltages $V = \pm 100$ mV were applied across the device to look for an odd in V shift and even in B shift in f_0. This approach to finding δf_0 eliminates shifts in the resonant frequency from V-independent bulk magnetization and V^2 Joule heating. There is no evidence of a quadratic dependence in $\delta f_0(B)$, as seen in Fig. 7(c). The Pt dummy cantilever thus shows no evidence of a Hall-like δf_0.

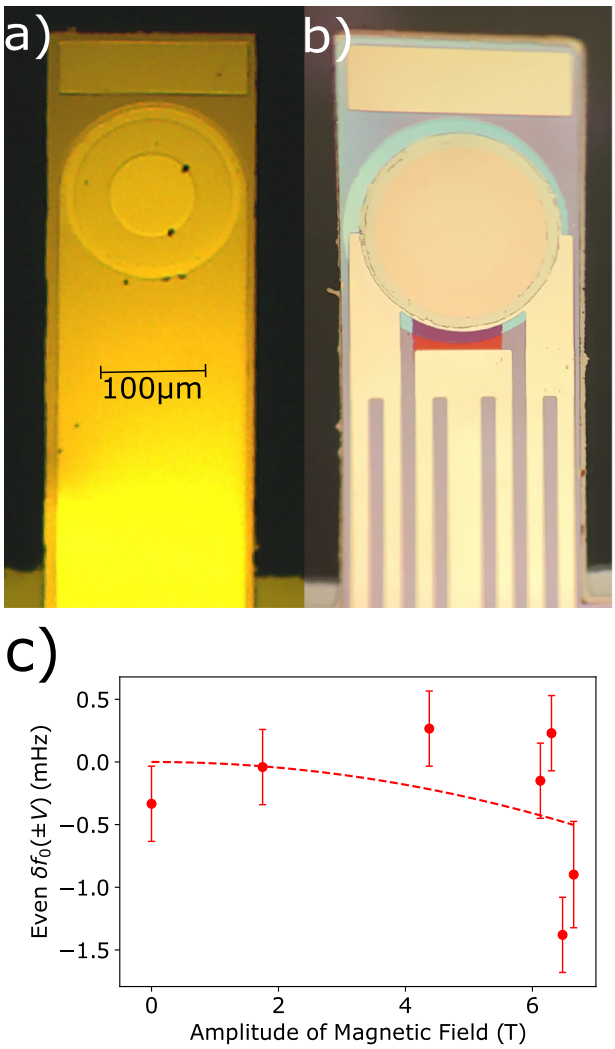

FIG. 7. (a) A dummy device with Pt wires used to look for systematic errors and noise bounds. (b) A Corbino disk cantilever with Ge as a test material. Note the pairs of wires for the inner and outer contacts to allow four wire measurements of the voltage across the disk. (c) Even component of δf_0 with the magnetic field for the Pt dummy cantilever. A quadratic fit for $\delta f_0(B)$ is plotted, with a fit coefficient of -5 ± 6 μHz/T^2. This fit coefficient is within 1σ of 0, and thus, there is no evidence of a Hall-like signal in the Pt dummy device.

C. Systematics tests: Insulating Ge device

Full Corbino disk cantilevers with evaporated amorphous Ge as a test material were also fabricated [Fig. 7(b)]. The insulating Ge serves both as a test for spurious δf_0 with voltage applied across the ring and as a means to verify that the full fabrication procedure did not create unintended electrical connections. The 3 μm thick Ge devices are both electrically and mechanically viable, with resistances of >20 MΩ and $Q \sim 250\,00$. Once more, there is no evidence of a Hall-like shift in f_0 at room temperature, finding $\delta f_0 = 88 \pm 91$ μHz in the zero-field and $\delta f_0 = 30 \pm 80$ μHz above a 0.3 T static magnet.

In conclusion, the dummy device tests demonstrate that design flaws creating Hall-like δf_0 have been eliminated. The Hall signal therefore may be distinguished by a voltage and magnetic field behavior from other shifts in f_0 in patterned Si cantilevers with Corbino disks.

D. Measurements of ITO Corbino disk

Corbino cantilevers with indium tin oxide (ITO) as a sample material were fabricated for first measurements of the Hall signal. ITO was chosen as an example of a disordered itinerant system, which can be tuned through a metal–insulator transition (MIT) by changing the tin and oxygen content. Here, we sputtered 50 nm of ITO with resistivity 3.5×10^{-3} Ω cm. Such ITO should exhibit $\sigma_{xy} > 1 \times 10^{-7}$ Ω^{-1} at 5 T.[23] Based on the observed carrier density in this system, such ITO should be in the vicinity of the MIT with $k_F \ell \lesssim 1$. With typical carrier density for this material, it is expected that $\rho_{xy}/\rho_{xx} \sim 10^{-4}$, which is on the borderline of standard methods of Hall effect detection.[23]

Cantilevers with ITO Corbino disks were tested to verify that a Hall signal can be seen. In an effort to improve future torque sensitivity, thinner 2 μm thick planar coaxial cantilevers were fabricated, as shown in Fig. 2. Figure 8 shows $\delta f_0(B)$ of an ITO Corbino disk cantilever in two data taking runs at 4.2 K. A linear component to $\delta f_0(B)$ caused by layer misalignment is clearly seen. The linear component is consistent with an alignment error of ~0.1 μm and

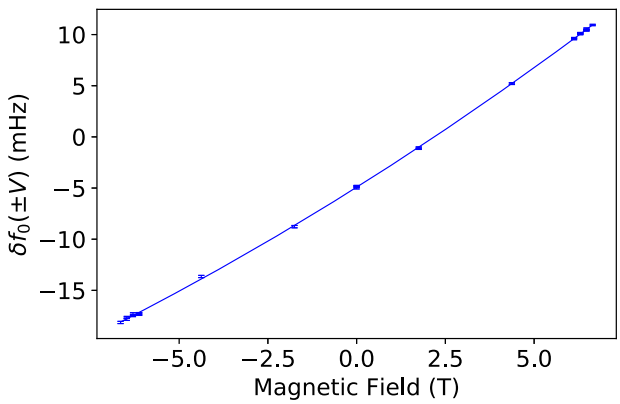

FIG. 8. Data and fit for $\delta f_0(B)$ with ±0.1 V applied across the second ITO cantilever. Each point comes from 170 fits of f_0 or approximately one hour of averaging time. Note the overriding linear dependence due to the patterning asymmetry of the current-carrying Pt wires. This can be used to compare A between cooldowns on the same cantilever or between cantilevers patterned on the same wafer.

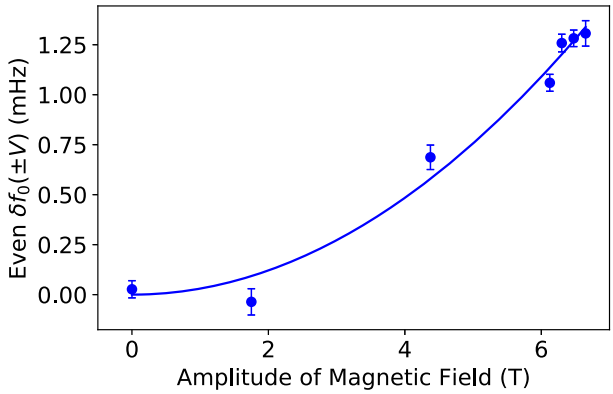

FIG. 9. Data and quadratic fit for the even component of $\delta f_0(B)$. The even component is defined by averaging the datapoints of Fig. 8 with the same magnetic field amplitude. There is a clear quadratic Hall signal in all cooldowns with sputtered ITO as a test material.

$A = 5 \times 10^{-18}$ kg m^2 on cooldown 2. After fitting to a second order polynomial and subtracting the linear and zero-field components, the Hall signal of the ITO can clearly be observed as a quadratic dependence in $\delta f_0(B)$ in Fig. 9. The quadratic fit coefficient is 30.7 ± 1.1 μHz/T^2. A second ITO cantilever was also tested. Using Eq. (7), at 5 T, the Hall conductivities of each cantilever are (2.0 ± 0.1) $\times 10^{-7}$ Ω^{-1} and (1.8 ± 0.3) $\times 10^{-7}$ Ω^{-1}, respectively. Converting back to resistivities, $\rho_{xy} \sim 0.1$ Ω or 5×10^{-7} Ω cm in 3D. This consistent result for σ_{xy} across different cantilevers, cooldowns, and data taking procedures is in agreement with the previous measurements of sputtered ITO and verifies that the observed quadratic dependence in $\delta f_0(B)$ is caused by the ITO Corbino disk. The small ratio of ρ_{xy}/ρ_{xx} and the ability to measure $\sigma_{xy} \sim 10^{-8}$ Ω^{-1} also demonstrate the effectiveness of this technique.

IV. SUMMARY

In summary, Corbino disk torque magnetometry is a new viable method for precisely measuring σ_{xy} in insulators. First, the initial challenge of fabricating high-Q cantilevers with patterned Corbino disks and contacts has been completed. The resonant frequency of such devices can be measured with a fractional uncertainty of ~10^{-9} after overnight averaging. This precision places current measurements within a factor of 10 of the theoretical noise floor for our cantilevers, likely due to electronics noise and the lack of special shielding. The Corbino disk cantilevers have also been tested for errors in fabrication, data collection procedures, and analysis protocols. These tests allowed for the elimination of systematic errors and spurious signals when applying the current and voltage across the disk. The Corbino disk cantilevers have also been used to measure σ_{xy} of sputtered ITO with a nominal resistivity of $\rho_{xx} \sim 3.5 \times 10^{-3}$ Ω cm. Such a measurement demonstrates the ability to detect the Hall effect in samples where $\rho_{xy}/\rho_{xx} \sim 10^{-5}$,[23] which is generally difficult to measure using standard techniques. Finally, even without experimental improvements, this new apparatus can improve upon measurements of σ_{xy} independent of ρ_{xx} as $T \to 0$ by a factor of >10^3.[19]

ACKNOWLEDGMENTS

This work was funded by the Army Research Office (Grant No. W911NF1710588) and the Gordon and Betty Moore Foundation through the Emergent Phenomena in Quantum Systems (EPiQS) Initiative (Grant No. GBMF4529). This work was also funded, in part, by a QuantEmX grant from ICAM and the Gordon and Betty Moore Foundation through Grant No. GBMF5305 to Seung Hwan Lee.

APPENDIX A: THEORETICAL NOISE FLOOR CALCULATION

For a cantilever response function $R(\omega, \omega_0)$ to an applied torque τ_{app}, the observed change in cantilever oscillation when the resonant frequency shifts by $\Delta\omega_0$ is

$$\Delta\theta_{sig}(\omega) = \tau_{app}(\omega)\frac{dR}{d\omega_0}\Delta\omega_0.$$

As seen in Fig. 4(a), τ_{app} is limited by the interferometer wavelength λ. For a cantilever of length L, the maximum angle of deflection over time t_{samp} is

$$\Delta\theta_{max} = \lambda/2L = \tau_{max}(\omega)R(\omega)2\pi/t_{samp}.$$

The largest possible signal for a single-frequency drive, therefore, is

$$\Delta\theta_{sig}(\omega) = \frac{\lambda t_{samp}}{2L}\frac{dR}{d\omega_0}\frac{1}{R(\omega)}\Delta\omega_0.$$

The fundamental experimental noise source is thermal vibration. By equipartition $k_BT = A\langle\theta^2(t)\rangle$ or assuming a white noise thermal drive τ_{therm},

$$\langle\theta^2(t)\rangle = \frac{\tau_{therm}^2}{t_{samp}}\int R^2(\omega)d\omega = \frac{k_BT}{A}.$$

Hence, with

$$\tau_{therm}(\omega) = \sqrt{2k_BTA\omega_0\frac{t_{samp}}{\pi Q}},$$

the noise response is

$$\Delta\theta(\omega) = \tau_{therm}(\omega)R(\omega, \omega_0, A, Q).$$

Setting the signal to noise ratio to 1, the minimum detectable frequency shift is

$$\Delta\omega_0 = \frac{4L}{\lambda t_{samp}}\sqrt{2\pi k_BTA\omega_0\frac{t_{samp}}{Q}}\min\left(\left|\left(\frac{dR}{d\omega_0}\right)^{-1}R^2(\omega)\right|\right)$$

or

$$\frac{\Delta\omega_0}{\omega_0} = \frac{2L}{\lambda}\sqrt{\frac{2k_BT\pi}{A\omega_0^3 t_{samp}Q}}.$$

This unitless noise bound has a simple physical explanation. Using that $\lambda/2L$ is the maximum angle of the driven cantilever, that $\omega_0 t_{samp}/2\pi$ is averaging time counted in a number of oscillations, and that narrower resonances will have less uncertain ω_0, the noise bound is truly

$$\frac{\Delta\omega_0}{\omega_0} = \sqrt{\frac{\text{Thermal Energy}}{\text{Driven Energy} * \text{Time in Oscillations} * Q}}.$$

Finally, using Eqs. (6) and (2),

$$\delta\sigma_{xy} = \frac{4L\ln(r_o/r_i)}{\lambda(r_o^2 - r_i^2)VB}\sqrt{\frac{2k_BTA\omega_0}{\pi t_{samp}Q}}.$$

The theoretical uncertainty bound can be compared to the present dummy cantilever data. Calculating A by observing the response magnitude to a known drive and using the vibrational temperature from equipartition along with Eq. (10), the best possible fractional uncertainty for such an experiment at 4.2 K should be $\sim 10^{-10}$. The fractional uncertainty without careful vibration isolation and with high electronics noise is currently $\sim 10^{-9}$ after overnight averaging.

APPENDIX B: FITTING FOR A, ω_0, AND Q

Fitting begins by Fourier transforming Eq. (3) to find

$$\theta(\omega) = \frac{1}{A\omega_0^2}\frac{\tau(\omega)}{\left(\frac{\omega_0^2-\omega^2}{\omega_0^2}\right) + i\frac{\omega}{\omega_0 Q}}. \tag{B1}$$

There is a small delay between the drive laser and the reference voltage controlling the laser, which makes the phase information unreliable. We correspondingly measure a power spectral density (PSD) of $\theta(\omega)$ and $\tau(\omega)$. This yields

$$PSD(\theta(\omega)) = \frac{1}{\left(A\omega_0^2\right)^2}\frac{PSD(\tau(\omega))}{\left(\frac{\omega_0^2-\omega^2}{\omega_0^2}\right)^2 + \left(\frac{\omega}{\omega_0 Q}\right)^2}. \tag{B2}$$

The observed cantilever response voltage (V_{res}) and reference drive voltage (V_{ref}) must be converted into θ and τ measurements. Assuming that all light is reflected, the force from the laser at power P_l is $2P_l/c$ and is applied at distance l along the cantilever. For the voltage control of the driving laser, $V_{max} = 5$ V translates to $P_{max} = 2$ mW. The laser torque in terms of the known drive voltage V_{ref}, therefore, is

$$\tau = \frac{2P_{max}l}{V_{max}c}V_{ref}. \tag{B3}$$

Additionally, using Eq. (8) and declaring $\theta_0 = 4\pi\Delta z_0/\lambda$,

$$\theta = \frac{\lambda}{2l\pi V_{pp}}\frac{V_{res}}{\sin(\theta_0)}. \tag{B4}$$

Note that θ_0 is known through the mean value of V_{res} during one drive and fit procedure.

Plugging into Eq. (B2),

$$PSD(V_{res}) = \left[\sin(\theta_0)\frac{4\pi V_{pp}P_{max}l^2}{V_{max}c\lambda}\right]^2\frac{1}{\left(A\omega_0^2\right)^2}\frac{PSD(V_{ref}(\omega))}{\left(\frac{\omega_0^2-\omega^2}{\omega_0^2}\right)^2 + \left(\frac{\omega}{\omega_0 Q}\right)^2}. \tag{B5}$$

Note that when fitting is performed, a simpler

$$PSD(V_{res}) = \frac{Z}{Q^2}\frac{PSD(V_{ref}(\omega))}{\left(\frac{\omega_0^2-\omega^2}{\omega_0^2}\right)^2 + \left(\frac{\omega}{\omega_0 Q}\right)^2} \tag{B6}$$

is used. Here, Z is roughly the ratio of the largest value of $PSD(V_{res})$ to the mean value of $PSD(V_{ref})$. Finally, Z can be inverted to find A, while ω_0 and Q are fit parameters. As an example, the A value of

5×10^{-18} kg m^2 used to analyze the ITO data in the final cooldown was found using $Z = 0.097$, $V_{pp} = 0.220$ V centered on $V = 0.185$ V, DC level for the fit of 0.09 V, $P_{max} = 0.5$ mW due to an attenuator, and $l = 550$ μm.

REFERENCES

[1] N. F. Mott, "Conduction in non-crystalline materials," Philos. Mag. **19**, 835–852 (1969).
[2] B. I. Shklovskii and A. L. Efros, *Electronic Properties of Doped Semiconductors*, 1st ed. (Springer-Verlag, Berlin Heidelberg, 1976).
[3] M. Steiner and A. Kapitulnik, "Superconductivity in the insulating phase above the field-tuned superconductor–insulator transition in disordered indium oxide films," Physica C **422**, 16–26 (2005).
[4] G. Sambandamurthy, L. Engel, A. Johansson, and D. Shahar, "Superconductivity-related insulating behavior," Phys. Rev. Lett. **92**, 107005 (2004).
[5] M. A. Paalanen, A. F. Hebard, and R. R. Ruel, "Low temperature insulating phases of uniformly disordered superconductors," Phys. Rev. Lett. **69**, 1604 (1992).
[6] M. P. A. Fisher, "Quantum phase transitions in disordered two-dimensional superconductors," Phys. Rev. Lett. **65**, 923–926 (1990).
[7] Y. Cao, V. Fatemi, A. Demir, S. Fang, S. L. Tomarken, J. Y. Luo, J. D. Sanchez-Yamagishi, K. Watanabe, T. Taniguchi, E. Kaxiras, R. C. Ashoori, and P. Jarillo-Herrero, "Correlated insulator behaviour at half-filling in magic-angle graphene superlattices," Nature **556**, 80–84 (2018).
[8] P. F. Hopkins, M. J. Burns, A. J. Rimberg, and R. M. Westervelt, "Magnetic-field-induced localization in degenerately doped *n*-type Ge," Phys. Rev. B **39**, 12708–12716 (1989).
[9] D. W. Koon and T. G. Castner, "Hall effect near the metal-insulator transition," Phys. Rev. B **41**, 12054–12070 (1990).
[10] L. Friedman and M. Pollak, "The hall effect in the variable-range-hopping regime," Philos. Mag. B **44**, 487–507 (1981).
[11] Y. M. Galperin, E. P. German, and V. G. Karpov, "Hall-effect under hopping conductivity conditions," Zh. Èksper. Teoret. Fiz. **99**, 343–356 (1991).
[12] P. Lou and T. Xiang, "Spin Hall current and two-dimensional magnetic monopole in a Corbino disk," arXiv:cond-mat/0501307 [cond-mat.mes-hall] (2005).
[13] R. B. Laughlin, "Quantized Hall conductivity in two dimensions," Phys. Rev. B **23**, 5632–5633 (1981).
[14] O. M. Von Corbino, Phys. Z. **12**, 561 (1911).
[15] M. Perfetti, "Cantilever torque magnetometry on coordination compounds: From theory to experiments," Coord. Chem. Rev. **348**, 171–186 (2017).
[16] J. Chiaverini, K. Yasumura, and A. Kapitulnik, "Microcantilever studies of angular field dependence of vortex dynamics in $Bi_2Sr_2CaCu_2O_{8-x}$," Phys. Rev. B **64**, 014516 (2001).
[17] A. C. Bleszynski-Jayich, W. E. Shanks, B. Peaudecerf, E. Ginossar, F. von Oppen, L. Glazman, and J. G. E. Harris, "Persistent currents in normal metal rings," Science **326**, 272–275 (2009).
[18] E. Finot, A. Passian, and T. Thundat, "Measurement of mechanical properties of cantilever shaped materials," Sensors **8**, 3497–3541 (2008).
[19] N. P. Breznay, M. A. Steiner, S. A. Kivelson, and A. Kapitulnik, "Self-duality and a Hall-insulator phase near the superconductor-to-insulator transition in indium-oxide films," Proc. Natl. Acad. Sci. U. S. A. **113**, 280–285 (2016).
[20] C. Gong, L. Li, Z. Li, H. Ji, A. Stern, Y. Xia, T. Cao, W. Bao, C. Wang, Y. Wang *et al.*, "Discovery of intrinsic ferromagnetism in two-dimensional van der Waals crystals," Nature **546**, 265–269 (2017).
[21] M. Majumder, M. Schmidt, H. Rosner, A. A. Tsirlin, H. Yasuoka, and M. Baenitz, "Anisotropic Ru_3^+ $4d^5$ magnetism in the α-$RuCl_3$ honeycomb system: Susceptibility, specific heat, and zero-field NMR," Phys. Rev. B **91**, 180401 (2015).
[22] K. A. Modic, M. D. Bachmann, B. J. Ramshaw, F. Arnold, K. R. Shirer, A. Estry, J. B. Betts, N. J. Ghimire, E. D. Bauer, M. Schmidt *et al.*, "Resonant torsion magnetometry in anisotropic quantum materials," Nat. Commun. **9**, 3975 (2018).
[23] F. Kurdesau, G. Khripunov, A. F. da Cunha, M. Kaelin, and A. N. Tiwari, "Comparative study of ITO layers deposited by DC and RF magnetron sputtering at room temperature," J. Non-Cryst. Solids **352**, 1466–1470 (2006).